

Model-independent Gamma-Ray Bursts Constraints on Cosmological Models Using Machine Learning

Bin Zhang^{1,2}, Huifeng Wang¹, Xiaodong Nong¹,
GuangZhen Wang¹, Puxun Wu^{3,4}, Nan Liang^{1*}

^{1*}Key Laboratory of Information and Computing Science Guizhou Province (School of Cyber Science and Technology), Guizhou Normal University, Guiyang, Guizhou 550025, China.

^{2*}School of Mathematical Sciences, Guizhou Normal University, Guiyang, Guizhou 550025, China.

^{3*}Department of Physics and Synergistic Innovation Center for Quantum Effects and Applications, Hunan Normal University, Changsha, Hunan 410081, China.

⁴Institute of Interdisciplinary Studies, Hunan Normal University, Changsha, Hunan 410081, China.

*Corresponding author(s). E-mail(s): liangn@bnu.edu.cn;
Contributing authors: binzhang@gznu.edu.cn; ; ; ; pxwu@hunnu.edu.cn;

Abstract

In this paper, we calibrate the luminosity relation of gamma-ray bursts (GRBs) with the machine learning (ML) algorithms from the Pantheon+ sample of type Ia supernovae in a cosmology-independent way. By using K-Nearest Neighbors (KNN) and Random Forest (RF) selected with the best performance in the ML algorithms, we calibrate the Amati relation (E_p - E_{iso}) relation with the A219 sample to construct the Hubble diagram of GRBs. Via the Markov Chain Monte Carlo numerical method with GRBs at high redshift and latest observational Hubble data, we find the results of constraints on cosmological models by using KNN and RF algorithms are consistent with those obtained from GRBs calibrated by using the Gaussian Process.

Keywords: gamma-ray bursts: general - cosmology: observations

1 Introduction

Type Ia supernovae (SNe Ia) have been often used as a standard candle with the maximum redshift observed at $z \sim 2.3$ (Scolnic et al. 2018; 2022). Therefore, observations of luminous objects at higher redshift than SNe Ia are required to explore the cosmic evolution at the high-redshift region. Gamma-ray bursts (GRBs) are the most intense bursts of high-energy gamma rays in a short time at high redshifts (the maximum redshift of GRB can reach at $z \sim 9$ (Cucchiara et al. 2011)). Utilizing the GRB's luminosity relations, which are connections between measurable properties of the instantaneous emission and the luminosity or energy (Fenimore & Ramirez-Ruiz 2000; Norris et al. 2000; Ghirlanda et al. 2004a; Yonetoku et al. 2004; Liang & Zhang 2005; Firmani et al. 2006; Dainotti et al. 2008; Tsutsui et al. 2009a), GRBs have been used as cosmic probe to study the evolutionary history of our universe and the properties of dark energy (Schaefer 2003; Dai et al. 2004; Ghirlanda et al. 2004b; Firmani et al. 2005; Xu et al. 2005; Liang & Zhang 2006; Wang & Dai 2006; Ghirlanda et al. 2006; Schaefer 2007).

In the early studies of GRB cosmology (Dai et al. 2004; Schaefer 2007), the luminosity relations of GRBs had usually been calibrated by assuming a certain cosmological model. Thus, the so-called circularity problem is encountered (Ghirlanda et al. 2006). In order to avoid this circularity problem, Liang et al. (2008) proposed a cosmological model-independent method to calibrate GRBs at low redshift interpolated from SNe Ia and built the GRB Hubble diagram at high redshift. Following the interpolation method used in (Liang et al. 2008), many works have constrained cosmological models with GRBs without any cosmological assumption, see, i. e. (Capozziello & Izzo 2008; 2009; Wei & Zhang 2009; Wei 2010; Liang et al. 2010; 2011; Wang et al. 2016; Liu et al. 2022b). On the other hand, the simultaneous method (Amati et al. 2008; Wang 2008) in which the parameters of the relationship and the cosmological model fitting simultaneously has been proposed to avoid the circularity problem. Recently, it is found that the GRB relation parameters are almost identical in all cosmological models, which seems to indicate that GRBs can be standardized within error bars (Khadka & Ratra 2020). It should be notice that GRB luminosity relations can be calibrated by using other observations. For example, Amati et al. (2019) proposed to calibrate GRB correlations by using the observational Hubble data (OHD) obtained with the cosmic chronometers (CC) method fitted by the Bézier parametric, and built up a Hubble diagram consisting of 193 GRBs with the Amati relation (the E_p - E_{iso} correlation)(Amati et al. 2002).¹ Following this method, several works have constrained cosmological models with the Amati relation calibrated by OHD (Montiel et al. 2021; Luongo & Muccino 2021b; 2023; Muccino et al. 2023).²

¹Besides the calibration method by using SN Ia and OHD, the mock data of gravitational waves (GWs) (Wang & Wang 2019), quasar sample (Dai et al. 2021) and the angular diameter distances of galaxy clusters (Gowri & Shantanu 2022) have also been used to calibrate GRBs.

²For recent GRB luminosity relations and the applications in cosmology, see e.g. Izzo et al. (2015); Dainotti & Amati (2018); Dainotti et al. (2020; 2022a); Xu et al. (2021; 2022; 2023); Hu et al. (2021); Wang et al. (2022); Liu et al. (2022a); Li et al. (2023), and Shirokov et al. (2020); Khadka & Ratra (2020); Khadka et al. (2021); Luongo & Muccino (2020); Demianski et al. (2021); Cao et al. (2022a;b); Liu et al. (2022b); Liang et al. (2022); Dainotti et al. (2022b;c; 2023); Li, Zhang & Liang (2023); Kumar et al. (2023); Mu et al. (2023); Bargiacchi, Dainotti & Capozziello (2023); Dinda (2023), and Shah et al. (2024); Cao & Ratra (2024); Wang, Li & Liang (2024). For reviews, see Luongo & Muccino (2021a); Moresco et al. (2022).

The reconstruction from cosmological data in the calibration of GRBs can be constructed in several ways. Similar to the interpolation method used in (Liang et al. 2008) and the Bézier parametric used in (Amati et al. 2019), GRBs are calibrated from the local data by using the polynomial fitting (Kodama et al. 2008; Tsutsui et al. 2009b), an iterative procedure (Liang & Zhang 2008), the local regression (Cardone et al. 2009; Demianski et al. 2017a), the cosmography methods (Capozziello & Izzo 2010; Gao et al. 2012), a two-steps method minimizing the use of SNe Ia (Izzo et al. 2015; Muccino et al. 2021), and the Padé approximation method (Liu & Wei 2015). Recently, the non-parametric method has been addressed to reconstruction of the dark energy, which can effectively reduce the errors of reconstructed results compared to the approaches mentioned in the above. Postnikov et al. (2014) studied the evolution of the cosmological equation of state in a nonparametric way with high redshift GRBs.

Gaussian Process (GP) is a powerful nonlinear interpolating tool without the need of specific models or parameters, which is a fully Bayesian approach that describes a distribution over functions with a generalization of Gaussian distributions to function space (Seikel et al. 2012a). GP approach has been used in various cosmological studies, see, e.g. (Seikel et al. 2012a;b; Seikel & Clarkson 2013; Busti et al. 2014; Li & Lin 2018). However, in GP analysis, it is typically assumed that the errors in observational data follow a Gaussian distribution (Seikel et al. 2012a), which may pose a substantial limitation when reconstructing functions from data. Wei & Wu (2017) found that GP exhibit sensitivity to the fiducial Hubble constant H_0 and the results are significantly impacted by H_0 . Zhou & Li (2019) proposed that GP should be used with caution for the reconstruction of OHD and SNe Ia. Furthermore, the results can be affected by the choose of the kernel functions, and there are a lot of kernel functions available that we can choose. Machine Learning (ML) algorithms are a set of technologies that learn to make predictions and decisions by training with a large amount of the observational data, which are a collection of processing units designed to identify underlying relationships in input data; therefore, when an appropriate network is chosen, the model created using ML can accurately depict the distribution of the input data in a completely data-driven way. The ML methods have shown outstanding performance in solving cosmological problems in both accuracy and efficiency to provide powerful tools and methods for cosmological research (Fluri et al. 2018; 2019; Arjona 2020; Wang et al. 2020; 2021; Xu et al. 2022; Escamilla-Rivera et al. 2020; Luongo & Muccino 2021b; Bengaly et al. 2023). Genetic Algorithms (GA) has been used to investigate the redshift evolution of the Cosmic Microwave Background (CMB) temperature (Arjona 2020), the distance duality relations (DDR) with gravitational wave (GW) (Hogg et al. 2020; Arjona et al. 2021), and the late-time cosmological tensions using redshift-space distortion data in the low-redshift background to show that phantom dark energy is more preferable than the cosmological constant (Gangopadhyay et al. 2023). Wang et al. (2020) proposed a new nonparametric approach for reconstructing a function from observational data using an Artificial Neural Network (ANN). Escamilla-Rivera et al. (2020) used the Recurrent Neural Networks (RNN) and the Bayesian Neural Networks (BNN) methods to reduce the computation load of expensive codes for dark energy models; these methods have subsequently been used to calibrate the GRB relations (Escamilla-Rivera et al. 2022; Tang et al. 2021; 2022).

Recently, [Luongo & Muccino \(2021b\)](#) explored three machine learning treatments (linear regression, neural network, and random forest) based on Bézier polynomials to alleviate the circularity problem with the Amati relation. The main issue in the calibration of GRBs is that we do not know a priori the correct curve to fitting data. The overall advantage on using machine learning has been discussed in ([Luongo & Muccino 2021b](#)): i) Healing degeneracy and over-fitting issues. Multiple models can fit the same data will lead to degeneracy in fitting data approaches, and the overall approach of ML overcomes those issues due to interpolation, polynomials with generic over-fitting treatments. ii) Speeding up the process of data adaption. ML can maintain the consistency of data, which automatically encapsulates data without postulation over the shapes and orders. The complexity of ML models turns out to intimately related to the number of data points. Therefore, the overall process of calibration can be improved. [Bengaly et al. \(2023\)](#) deployed ML algorithms to measure the H_0 through regression analysis as Extra-Trees, ANN, Gradient Boosting, and Support Vector Machines (SVM), and found that the SVM exhibits the best performance in terms of bias-variance tradeoff in most cases, showing itself a competitive cross-check to GP.

More recently, [Khadka et al. \(2021\)](#) compiled a total 220 GRBs (the A220 sample) to derive the correlation and cosmological model parameter constraints simultaneously. By using the GP method, [Liang et al. \(2022\)](#) calibrated the Amati relation with the A219 GRB sample³ from the Pantheon sample ([Scolnic et al. 2018](#)) which contains 1048 SNe, and constrained cosmological models in flat space with GRBs at high redshift and OHD via the Markov Chain Monte Carlo (MCMC) numerical method. [Li, Zhang & Liang \(2023\)](#) calibrated GRBs from the latest OHD to construct the GRB Hubble diagram and constrained Dark Energy models with GRBs at high redshift and SNe Ia in a flat space. [Mu et al. \(2023\)](#) used the Pantheon+ sample ([Scolnic et al. 2022](#)), which contains 1701 SNe light curves of 1550 spectroscopically confirmed SNe Ia, for calibrating the Amati relation to reconstruct cosmography parameters. [Xie et al. \(2023\)](#) used the Pantheon+ sample to calibrate the Amati relation from the latest 221 GRB sample ([Jia et al. 2022](#)).

In this work, we calibrate the Amati relation with the A219 GRB data ([Liang et al. 2022](#)) at low redshift from the Pantheon+ SNe Ia sample ([Scolnic et al. 2022](#)) using the ML algorithms. Combining the high redshift GRB data with the latest OHD, we constrain cosmological models in a flat space with MCMC numerical method. We also compare the results of ML and GP methods.

2 Reconstructing the apparent magnitude redshift Relation from Pantheon+

In this section, we use ML algorithms to fit SNe Ia data set to reconstruct the apparent magnitude-redshift ($m - z$) relation. To implement the regression models of ML algorithms, we use scikit-learn⁴, which offers a variety of ML classification and regression models to choose, e.g., Linear Regression(LR), Lasso Regression(Lasso), Random

³Removed GRB051109A, which are counted twice in the A220 sample ([Khadka et al. 2021](#)).

⁴<https://scikit-learn.org/stable/index.html>

Forest (RF), Support Vector Regression (SVR), and K-Nearest Neighbors (KNN). In order to estimate the performance of different ML algorithms that reduce the residuals between real and fitting data, we use the values of the mean squared error (MSE), which are given by

$$\text{MSE} = \frac{1}{N} \sum_{i=1}^N (Y_i - \hat{Y}_i)^2. \quad (1)$$

We also select MSE as the evaluation index and utilize the hyperparameter optimization method (GridSearchCV⁵) provided by scikit-learn to determine optimal hyperparameters for the ML algorithms.⁶

The Pantheon+ dataset consists of 1701 light curves of 1550 unique spectroscopically confirmed SNe Ia ($z = 0.00122$ to 2.26137), with a table of size 1701×47 (Pantheon+SH0ES.dat⁷). It also consists of a 1701×1701 covariance matrix $C_{\text{stat+sys}}$ which represents the covariance between SN Ia due to systematic and statistical uncertainties. Although ML algorithms in scikit-learn are able to predict apparent magnitude of SN Ia at a given redshift, they do not provide their uncertainties. Following Bengaly et al. (2023), we first develop a Monte Carlo-bootstrap (MC-bootstrap) method to generate 1000 instances of data (m_{MC}) with the initial candidate sample being drawn from the distribution of Pantheon+'s apparent magnitude (m_{obs}) and covariance matrix C . Based on Monte Carlo sampling datasets, 1000 iterations of ML algorithms training are conducted to predict each redshift of the testing set by the objective functions. The average of the prediction results of the objective functions is taken to obtain the m_{pred} value, and the standard deviation is taken to obtain the error $\sigma_{m_{\text{pred}}}$ value. The data flow diagram of ML in our study is shown in Fig. 1.

It should be noted that the Pantheon+ sample do not use SNe from SNLS at $z > 0.8$ due to sensitivity to the U band in model training, therefore the Pantheon+ statistics between $0.8 < z < 1.0$ are lower than that of Pantheon (Scolnic et al. 2018) and the Joint Light-curve Analysis (JLA, Betoule et al. (2014)). We selected a series of different redshift splits (from 0.6 to 2.26, taking a point every 0.2) in the training phase of each ML algorithms to determine the reliable redshift splits of the Pantheon+ sample to calibrate GRBs. For each redshift split, we take the SNe Ia $z < z_{\text{split}}$ to calculate MSE, and the results with the ML algorithms are shown in Fig. 2. The results with the ML algorithms at critical redshifts (e.g. $z = 0.8, 1.4, 2.26$) are listed in Tab. 1. From Fig. 2, Tab. 1 (the subgraph of Fig. 2), we find that KNN and RF methods show the relatively better performances in redshift splits from 0.6 to 2.26; and all ML methods except SVM achieve the best values at $z = 0.8$, which are consistent with the redshift point empirically chosen in Mu et al. (2023) and Xie et al. (2023) from Pantheon+ sample. In Fig. 3, we plot the reconstruction of the apparent magnitude from Pantheon+ by KNN and RF methods with the relatively better performances reconstructed using the optimal hyperparameters⁸.

⁵https://scikit-learn.org/stable/modules/generated/sklearn.model_selection.GridSearchCV.html

⁶In grid search, we assess various hyperparameter combinations for each ML algorithms and utilize the 5-fold cross-validation method to select the one that minimizes MSE as the final configuration

⁷https://github.com/PantheonPlusSH0ES/DataRelease/tree/main/Pantheon%2B_Data/4_DISTANCES_AND_COVAR

⁸When training machine learning algorithms based on each of 1000 Monte Carlo sampled datasets, we employ the GridSearchCV method to determine the optimal hyperparameter values.

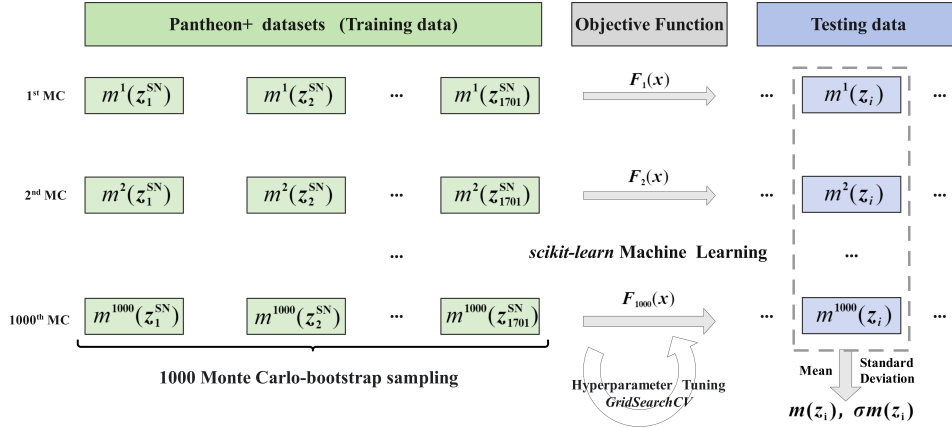


Fig. 1 The architecture of machine learning algorithms to fit Pantheon+ data. To estimate the uncertainty of the apparent magnitude, we use a Monte Carlo-bootstrap method, which sample the apparent magnitude corresponding to each redshift of SN Ia data by assuming a normal distribution.

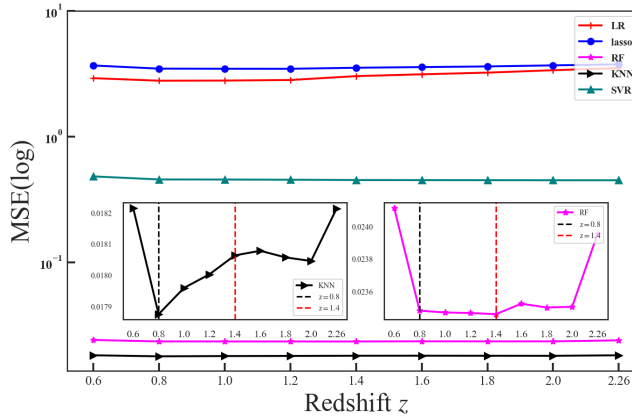


Fig. 2 The values of MSE by the multiple ML algorithms fitting Pantheon+ data at redshift splits. Inside plot: Highlight the respective performances of the top two methods with minimal MSE (from left to right: KNN and RF) at redshift splits.

3 Calibration of the Amati relation and the GRB Hubble diagram

For GRB data set, we use the A219 sample (Liang et al. 2022) with one point GRB051109A removed in the A220 sample (Khadka et al. 2021), which includes the A118 data set with the smallest intrinsic dispersion, as well as 102 data set (A102) from 193 GRBs analyzed by Amati et al. (2019) and Demianski et al. (2017a). We divide A219 sample into two subsamples, i.e., the low-redshift GRB sample ($z < 0.8$), which consists of 37 GRBs, and the high-redshift sample ($z > 0.8$), which consists of

Table 1 The corresponding MSE of the multiple ML algorithms from Pantheon+ at critical redshifts $z_{\text{split}} = 0.8, 1.4, 2.26$.

ML	$z < 0.8$ (1671 SNe)	$z < 1.4$ (1693 SNe)	$z < 2.26$ (1701 SNe)
Lasso Regression	3.4771	3.5338	3.7608
Linear Regression	2.7869	3.0312	3.5102
Support Vector Regression	0.4565	0.4516	0.4497
Random Forest	0.0234	0.0234	0.0239
K-Nearest Neighbors	0.0178	0.0180	0.0182

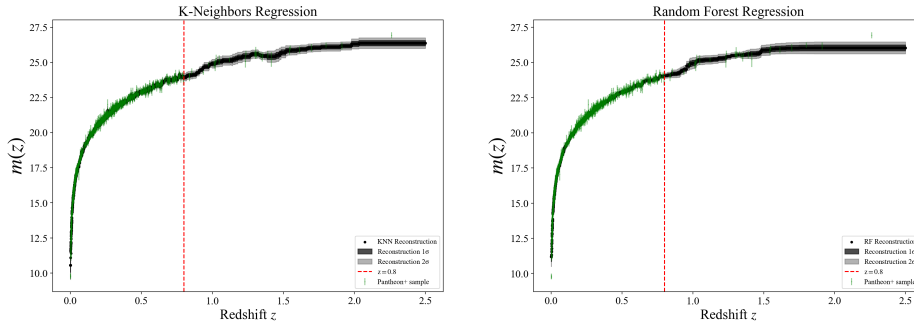


Fig. 3 Reconstruction of the apparent magnitude from the Pantheon+ data set by KNN (left panel) and RF (right panel). The green dots represent Pantheon+ data points with 1σ error bars. The model reconstructed center value (black point) and the corresponding 1σ and 2σ uncertainties (shaded area). The red dotted line marks the redshift split point corresponding to the minimum MSE at $z = 0.8$.

182 GRBs. The Amati relation which connects the spectral peak energy (E_p) and the isotropic equivalent radiated energy (E_{iso}) is expressed as

$$y = a + bx \quad (2)$$

where $y \equiv \log_{10} \frac{E_{\text{iso}}}{1 \text{ erg}}$, $x \equiv \log_{10} \frac{E_p}{300 \text{ keV}}$, a and b are free coefficients; E_{iso} and E_p can be respectively expressed as:

$$E_{\text{iso}} = 4\pi d_L^2(z) S_{\text{bolo}}(1+z)^{-1}, \quad E_p = E_p^{\text{obs}}(1+z) \quad (3)$$

where E_p^{obs} is the observational value of GRB spectral peak energy and S_{bolo} is observational value of bolometric fluence. The luminosity distance (d_L) is related the distance modulus (μ), $\mu = m - M = 5 \log \frac{d_L}{\text{Mpc}} + 25$. In order to express the GRB relation direct from the apparent magnitude m , we introduce a new coefficient a' to rewrite the Amati relation by

$$y' = a' + bx \quad (4)$$

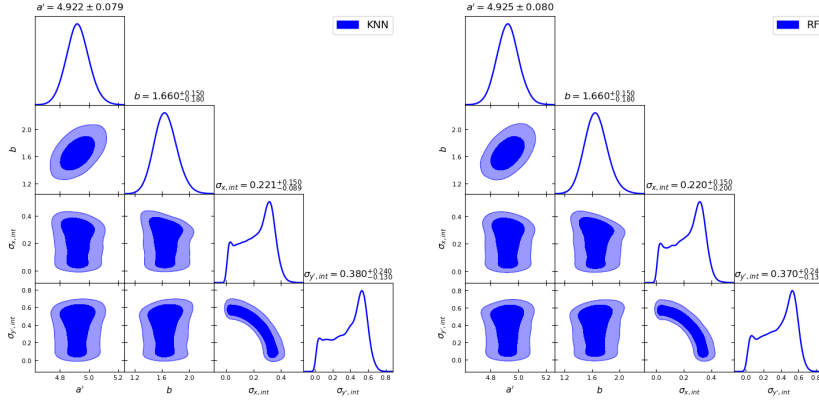


Fig. 4 The MCMC numerical fitting results (the intercept a' , the slope b and the intrinsic scatter along the x -axis and y' -axis $\sigma_{x,\text{int}}$ and $\sigma_{y',\text{int}}$) of the Amati relation in the A219 GRB sample at $z < 0.8$ (37 GRBs) by the likelihood method (Reichart 2001) by KNN (left panel) and RF (right panel).

where $y' = \log_{10}[(1+z)^{-1}(S_{\text{bolo}}/1\text{ergcm}^{-2})] + \frac{2}{5}m$, $a' = a + 2(\frac{M}{5} + 5) - \log_{10}[4\pi(\text{Mpc/cm}^2)^2]$ and b are free coefficients needing to be calibrated from the GRBs observed data in the formula. Therefore, we can calibrate the Amati relation without assuming any prior values of M .

We use likelihood function methods (Reichart 2001) to fit the parameters of Amati relation which can be written as (Lin et al. 2016; Li, Zhang & Liang 2023)

$$\mathcal{L}_R \propto \prod_{i=1}^{N_1} \frac{\sqrt{1+b^2}}{\sigma} \times \exp\left[-\frac{[y'_i - y'(x_i, z_i; a', b)]^2}{2\sigma^2}\right] \quad (5)$$

Here $\sigma = \sqrt{\sigma_{\text{int}}^2 + \sigma_{y',i}^2 + b^2\sigma_{x,i}^2}$, the intrinsic scatter $\sigma_{\text{int}} = \sqrt{\sigma_{y',\text{int}}^2 + b^2\sigma_{x,\text{int}}^2}$, in which $\sigma_{x,\text{int}}$ and $\sigma_{y',\text{int}}$ are the intrinsic scatter along the x -axis and y' -axis. The likelihood function proposed by Reichart (2001) has the advantage of not requiring the arbitrary choice of an independent variable from E_p and E_{iso} (Amati & Della Valle 2013; Li, Zhang & Liang 2023).⁹

The python package `emcee` (Foreman-Mackey et al. 2013) is used to implement the MCMC numerical fitting. The best fitting parameters a' , b , σ_{int} by KNN and RF methods from the A219 sample at redshift $z < 0.8$ are shown in Fig. 4 and Tab. 2. For comparison, we also use the `GaPP` package¹⁰ of the well-known Gaussian process with the squared exponential covariance function (Seikel et al. 2012a). From Tab. 2, We find that the results of GP are consistent with previous analyses that obtained in

⁹The use of the D'Agostini (2005) likelihood ($\mathcal{L}_D \propto \prod_{i=1}^{N_1} \frac{1}{\sigma^2} \times \exp\left[-\frac{[y_i - y(x_i, z_i; a, b)]^2}{2\sigma^2}\right]$, here $\sigma = \sqrt{\sigma_{\text{int}}^2 + \sigma_{y,i}^2 + b^2\sigma_{x,i}^2}$, σ_{int} is the intrinsic scatter of GRBs, $\sigma_x = \frac{1}{\ln 10} \frac{\sigma_{E_p}}{E_p}$, $\sigma_y = \frac{1}{\ln 10} \frac{\sigma_{E_{\text{iso}}}}{E_{\text{iso}}}$, and $\sigma_{E_{\text{iso}}} = 4\pi d_L^2 \sigma_{S_{\text{bolo}}} (1+z)^{-1}$.) may introduce a subjective bias on the choice of the independent variable in the analysis. The Bivariate Correlated Errors and intrinsic Scatter (BCES) method (Akritas & Bershady 1996) used in recent Fermi data (Wang & Liang 2024) take into account the possible intrinsic scatter of the data.

¹⁰<https://github.com/astrobenjaly/GaPP>

Table 2 The best-fitting results (the intercept a' , the slope b and the intrinsic scatter σ_{int}) of the Amati relation in the A219 GRB sample at $z < 0.8$.

Likelihood	Methods	Datasets	a'	b	σ_{int}
D'Agostini (2005)	KNN	37GRBs ($z < 0.8$)	$4.830^{+0.074}_{-0.074}$	$1.26^{+0.15}_{-0.15}$	0.551
	RF	37GRBs ($z < 0.8$)	$4.831^{+0.074}_{-0.074}$	$1.26^{+0.15}_{-0.15}$	0.551
	GaPP	37GRBs ($z < 0.8$)	$4.880^{+0.11}_{-0.11}$	$1.26^{+0.22}_{-0.22}$	0.574
Reichart (2001)	KNN	37GRBs ($z < 0.8$)	$4.922^{+0.079}_{-0.079}$	$1.66^{+0.15}_{-0.18}$	0.527
	RF	37GRBs ($z < 0.8$)	$4.925^{+0.080}_{-0.080}$	$1.66^{+0.15}_{-0.18}$	0.519
	GaPP	37GRBs ($z < 0.8$)	$4.974^{+0.081}_{-0.081}$	$1.67^{+0.15}_{-0.18}$	0.534

Mu et al. (2023) using GaPP from SNe Ia at $z < 0.8$; and the fitting results by GP are consistent with that by KNN and RF methods in 1σ uncertainty, which indicate that ML methods are competitive to GP method.

In order to derive the luminosity distances of GRBs at high-redshift to build the GRB Hubble diagram, we assume that the calibration results of the Amati relation at low-redshift are valid at high-redshift.¹¹ We utilize the calibration results obtained through the likelihood (Reichart 2001) to construct the GRB Hubble diagrams at $z \geq 0.8$ for avoiding any bias in the selection of independent variables. The Hubble diagram (the apparent magnitude verse the redshift) of A219 GRB sample by KNN and RF is plotted in Fig. 5. The uncertainty of the apparent magnitude with the Amati relation can be expressed as

$$\sigma_m^2 = \left(\frac{5}{2}\sigma_{y'}(a', b, x, \sigma_{\text{int}})\right)^2 + \left(\frac{5}{2\ln 10} \frac{\sigma_{S_{\text{bolo}}}}{S_{\text{bolo}}}\right)^2 \quad (6)$$

where

$$\sigma_{y'}^2(a', b, \sigma_{\text{int}}, x) = \sigma_{\text{int}}^2 + \left(\frac{b}{\ln 10} \frac{\sigma_{E_p}}{E_p}\right)^2 + \sigma_{y'}^2(a', b); \quad (7)$$

Here $\sigma_{y'}^2(a', b) = \left(\frac{\partial y'}{\partial a'}\right)^2 \sigma_{a'}^2 + \left(\frac{\partial y'}{\partial b}\right)^2 \sigma_b^2 + 2\left(\frac{\partial y'}{\partial a'}\right)\left(\frac{\partial y'}{\partial b}\right)C_{a'b}^{-1}$, and the inverse of covariance matrix from the fitting coefficients is $(C^{-1})_{a'b} = \left(\frac{\partial L^2}{\partial a' \partial b}\right)$.

4 Constraints on cosmological models

We use the GRB data in the Hubble diagram at high-redshift to constrain cosmological models. The cosmological parameters can be fitted by minimizing the χ^2 statistic. The

¹¹It should be noted that whether the luminosity relations of GRB are redshift dependent or not is still under debate. The possible evolutionary effects in GRB relations have been discussed in many works (Lin et al. 2016; Wang et al. 2017; Demianski et al. 2017a; 2021; Dai et al. 2021; Tang et al. 2021). Khadka et al. (2021) found that the Amati relation is independent of redshift within the error bars. (Liu et al. 2022a;b) proposed the improved Amati relation by accounting for evolutionary effects via copula, and found that a redshift evolutionary correlation is slightly favored. Jia et al. (2022) found no statistically significant evidence for the redshift evolution with the Amati relation from the analysis of data in different redshift intervals with the 221 GRB sample. Kumar et al. (2023) calibrated the Amati relation into five redshift bins and find that GRBs seem to evolve with redshift. Further examinations of possible evolutionary effects should be required for considering GRBs as standard candles for a cosmological probe.

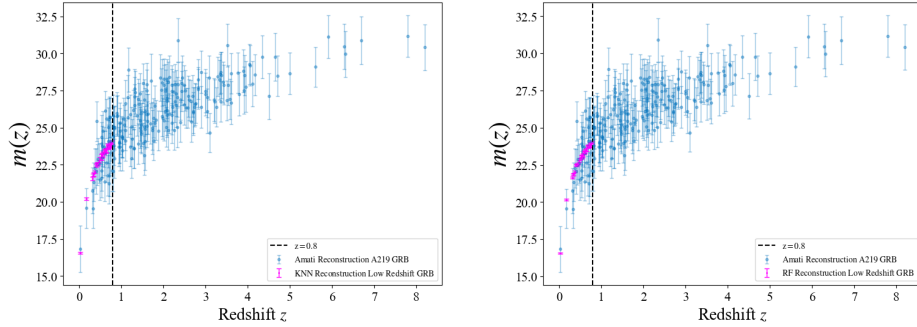


Fig. 5 GRB Hubble diagram with the A219 data set. GRBs at $z < 0.8$ are obtained by the KNN (left panel) and RF (right panel) from the Pantheon+ data, while GRBs with $z \geq 0.8$ (blue points) are obtained by the Amati relation calibrated with GRBs at $z < 0.8$ by the likelihood method (Reichert 2001). The black dashed line denotes $z = 0.8$.

χ^2 function for the GRB data can be expressed as

$$\chi_{\text{GRB}}^2 = \sum_{i=1}^{n_1} \left[\frac{m_{\text{obs}}(z_i) - m_{\text{th}}(z_i; P, H_0)}{\sigma_{m_i}} \right]^2. \quad (8)$$

Here, $n_1 = 182$ is the number of GRBs at $z > 0.8$ in the A219 sample, m_{obs} is the observational value of the apparent magnitude with its error σ_{m_i} , and m_{th} is the theoretical value of the apparent magnitude calculated from the cosmological parameters P ,

$$m_{\text{th}}(P) = 5 \log \frac{d_L(P)}{\text{Mpc}} + 25 + M = 5 \log_{10} D_L(P) - \mu_0 + M, \quad (9)$$

where $\mu_0 = 5 \log_{10} h + 42.38$, $h = H_0/(100 \text{ km/s/Mpc})$, H_0 is the Hubble constant, the unanchored luminosity distance $D_L(P) = d_L(P)H_0$.

We consider three the dark energy (DE) models for a flat space¹², the Λ CDM model with the Equation of State (EoS) $w = -1$, the w CDM model ($w = \text{const}$), and the CPL model evolving with redshift with a parametrization EoS ($w = w_0 + w_a z/(1+z)$). In a flat space,

$$d_{L;\text{th}} = \frac{c(1+z)}{H_0} \int_0^z \frac{dz'}{E(z')} \quad (10)$$

¹²The cosmological models have been usually constrained with flat spatial curvature. It should be noted that recently works constrain nonspatially flat models with GRBs and results are promising (Khadka et al. 2021; Cao et al. 2022a; Luongo & Muccino 2023).

Table 3 Joint constraints on parameters of Ω_m , h , w_0 and w_a for the flat Λ CDM model, w CDM model, and CPL model, obtained by using the KNN, RF, and GaPP methods with 182 GRBs ($z > 0.8$) + 32 OHD data.

Models	Methods	Ω_m	h	w_0	w_a	Δ AIC	Δ BIC
Λ CDM	KNN	$0.329^{+0.046}_{-0.068}$	$0.709^{+0.038}_{-0.038}$	-	-	-	-
	RF	$0.330^{+0.046}_{-0.067}$	$0.709^{+0.038}_{-0.038}$	-	-	-	-
	GaPP	$0.329^{+0.048}_{-0.071}$	$0.696^{+0.039}_{-0.039}$	-	-	-	-
w CDM	KNN	$0.301^{+0.080}_{-0.057}$	$0.721^{+0.048}_{-0.065}$	$-1.13^{+0.62}_{-0.38}$	-	1.4	4.8
	RF	$0.300^{+0.081}_{-0.057}$	$0.721^{+0.050}_{-0.064}$	$-1.12^{+0.60}_{-0.41}$	-	1.5	4.8
	GaPP	$0.294^{+0.090}_{-0.060}$	$0.706^{+0.050}_{-0.070}$	$-1.10^{+0.67}_{-0.35}$	-	1.4	4.7
CPL	KNN	$0.341^{+0.072}_{-0.072}$	$0.713^{+0.051}_{-0.051}$	$-1.03^{+0.60}_{-0.45}$	$-0.97^{+0.58}_{-0.58}$	3.7	10.5
	RF	$0.340^{+0.072}_{-0.072}$	$0.713^{+0.053}_{-0.069}$	$-1.04^{+0.59}_{-0.48}$	$-0.97^{+0.58}_{-0.58}$	3.1	9.8
	GaPP	$0.338^{+0.074}_{-0.074}$	$0.701^{+0.053}_{-0.069}$	$-1.05^{+0.59}_{-0.50}$	$-0.95^{+0.57}_{-0.57}$	3.7	10.5

here c is the speed of light, $E(z) = [\Omega_M(1+z)^3 + \Omega_{DE}X(z)]^{1/2}$, and $X(z) = \exp[3 \int_0^z \frac{1+w(z')}{1+z'} dz']$, which is determined by,

$$X(z) = \begin{cases} 1, & \Lambda\text{CDM} \\ (1+z)^{3(1+w_0)}, & w\text{CDM} \\ (1+z)^{3(1+w_0+w_a)} e^{-\frac{3w_a z}{1+z}}, & \text{CPL} \end{cases} \quad (11)$$

The OHD can be obtained from the galactic age differential method (Jimenez & Loeb 2002), which have advantages to constrain cosmological parameters and distinguish dark energy models. In our analysis, we also use the latest OHD (Li, Zhang & Liang 2023) to constrain cosmological models, including the 31 Hubble parameter measurements at $0.07 < z < 1.965$ (Stern et al. 2010; Moresco et al. 2012; 2015; 2016; Zhang et al. 2014; Ratsimbazafy et al. 2017), and a new point at $z = 0.80$ proposed by Jiao et al. (2023) in a similar approach. In this work, we also use the 31 OHD at $0.07 < z < 1.965$ and one point at $z = 0.75$ from Jiao et al. (2023).¹³ The total OHD contain 32 data, including 15 correlated measurements (Moresco et al. 2012; 2015; 2016) with the covariance matrix (Moresco et al. 2020). The χ^2 function for the OHD is,

$$\chi_{\text{OHD}}^2(\mathbf{p}) = \Delta \hat{H}^T \mathbf{C}_H^{-1} \Delta \hat{H} + \chi_{\text{uncor}}^2. \quad (12)$$

Here the difference vector for the 15 correlated measurements between the observed data (H_{obs}) and the theoretical values ($H_{\text{th}}(z; \mathbf{p}) \equiv H_0 \sqrt{\Omega_M(1+z)^3 + \Omega_{DE}X(z)}$) is: $\Delta \hat{H} = H_{\text{th}}(z; \mathbf{p}) - H_{\text{obs}}(z)$; \mathbf{C}_H^{-1} is the inverse of the covariance matrix; and the χ^2

¹³It should be noted that Borghi et al. (2022) obtained another new OHD at $z = 0.75$. Considering these two measurements are not fully independent and their covariance is not clear, we only use the point Jiao et al. (2023), which takes advantage of the $1/\sqrt{2}$ fraction of systematic uncertainty. One could either use the data from Borghi et al. (2022) alternatively with other 31 OHD to investigate cosmology (Cao & Ratra 2022; Muccino et al. 2023; Favale et al. 2023; Kumar et al. 2023).

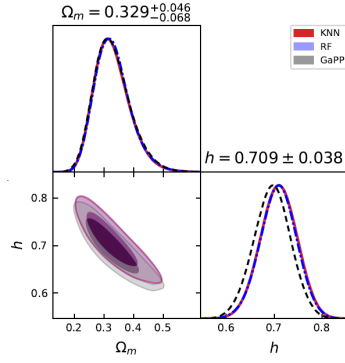


Fig. 6 Joint constraints on parameters of Ω_m , h for the flat Λ CDM model by the KNN, RF and GaPP methods with 182 GRBs ($z > 0.8$) + 32 OHD.

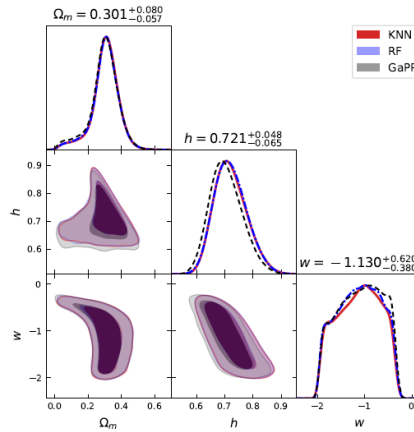


Fig. 7 Joint constraints on parameters of Ω_m , h , and w_0 for the flat w CDM by the KNN, RF and GaPP methods with 182 GRBs ($z > 0.8$) + 32 OHD.

function for the 17 uncorrelated measurements is

$$\chi_{\text{uncor}}^2 = \sum_{i=1}^{17} [H_{\text{th}}(z_i; \mathbf{p}) - H_{\text{obs}}(z_i)]^2 / \sigma_{H,i}^2 \quad (13)$$

The total χ^2 with the joint data of GRB+OHD can be expressed as $\chi_{\text{total}}^2 = \chi_{\text{GRB}}^2 + \chi_{\text{OHD}}^2$. The python package `emcee` (Foreman-Mackey et al. 2013) for the MCMC numerical fitting is used to constrain DE models from the GRB. The cosmological parameters can be fitted by using the minimization χ^2 method through MCMC method. The joint results from 182 GRBs (A219) $z > 0.8$ with 32 OHD are shown in Fig. 6 (Λ CDM), Fig. 7 (w CDM) and Fig. 8 (CPL).

We find the joint results by the KNN method are most identical with results by the RF algorithm with 182 GRBs at $0.8 < z < 8.2$ in the A219 sample and 32 OHD.

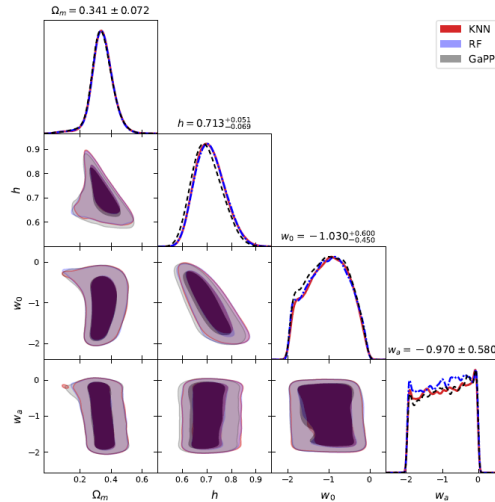


Fig. 8 Constraints on parameters of Ω_m , h , w_0 and w_a for the flat CPL model by the KNN, RF and GaPP methods with 182 GRBs ($z > 0.8$) + 32 OHD.

By the KNN method, we obtained $\Omega_m = 0.329^{+0.046}_{-0.068}$, $h = 0.709^{+0.038}_{-0.038}$ for the flat Λ CDM model; $\Omega_m = 0.301^{+0.080}_{-0.057}$, $h = 0.721^{+0.048}_{-0.065}$, $w = -1.13^{+0.62}_{-0.38}$ for the flat w CDM model; and $\Omega_m = 0.341^{+0.072}_{-0.072}$, $h = 0.713^{+0.051}_{-0.051}$, $w_0 = -1.03^{+0.60}_{-0.45}$, $w_a = -0.97^{+0.58}_{-0.58}$ for the CPL model at the 1σ confidence level, which favor a possible DE evolution ($w_a \neq 0$). For comparison, we also use the calibration results of GaPP to constrain cosmological models, which are consistent with the results by KNN and RF with slight difference. We also find that the results by GP from the Pantheon+ data at $z < 0.8$ are consistent with previous analyses that obtained in Liang et al. (2022) using GP from the Pantheon data at $z < 1.4$ for the Λ CDM model and the w CDM model.

For the well-known H_0 tension (Hu & Wang 2023), H_0 with a redshift evolving is an interesting idea¹⁴. Jia et al. (2023) found that H_0 value is consistent with that measured from the local data at low redshift and drops to the value measured from the CMB at high redshift. Moreover, Malekjani et al. (2023) found the evolving (H_0 , Ω_m) values above $z = 0.7$ in Pantheon+ sample. Compared to the fitting results from CMB data based on the Λ CDM model at very high-redshift ($H_0 = 67.36 \text{ km s}^{-1} \text{ Mpc}^{-1}$, $\Omega_m = 0.315$) (Planck Collaboration 2020) and SNe Ia at very low-redshift ($H_0 = 74.3 \text{ km s}^{-1} \text{ Mpc}^{-1}$, $\Omega_m = 0.298$) (Scolnic et al. 2022), we find that the H_0 value with GRBs by ML at $0.8 \leq z \leq 8.2$ and OHD at $z \leq 1.975$ seems to favor the one from the Planck observations, and the Ω_m value of our results for the flat Λ CDM model is consistent with the CMB observations at the 1σ confidence level.

In order to compare the different cosmological models and ML algorithms, we compute the values of the Akaike information criterion (AIC; Akaike et al. (1974; 1981)) and the Bayesian information criterion (BIC; Schwarz et al. (1978)), respectively:

¹⁴See e. g. Wong et al. (2020), Krishnan et al. (2020), Krishnan et al. (2021), Dainotti et al. (2021) for earlier work.

AIC = $2p - 2\ln(\mathcal{L})$, BIC = $p \ln N - 2\ln(\mathcal{L})$; where \mathcal{L} is the maximum value of the likelihood function, p is the number of free parameters in a model, and N is the number of data. We find that the results of ΔAIC and ΔBIC by KNN, RF and GP methods indicate that the ΛCDM model is favoured respect to the $w\text{CDM}$ model and the CPL model, which are consistent with the previous analyses (Amati et al. 2019) obtained from the 193 GRBs by using the OHD at $z < 1.975$ through the Bézier parametric curve combined with 740 SNe Ia.

5 Results of the Dainotti relation

GRB relations of the prompt emission phase involving the X-ray afterglow plateau phase exist less variability in its features (Dainotti et al. 2008; Cardone et al. 2009). In this section, we also investigate the Dainotti relation¹⁵ by the ML algorithms for comparison.

The Platinum sample (Dainotti et al. 2020) listed in Table A1 of Cao et al. (2022a) are used to calibrate the Dainotti relation by the KNN and RF methods. The 2D Dainotti relation which connects the X-ray luminosity L_X and the rest-frame time at the end of the plateau emission T_X^* is expressed as (Cao et al. 2022a)

$$\log_{10} L_X = C_0 + a \log_{10} T_X^* \quad (14)$$

where C_0 and a are free coefficients, L_X can be calculated by

$$L_X = 4\pi d_{L,\text{rec}}^2(z) F_X (1+z)^{\beta-1}, \quad (15)$$

where F_X is the measured gamma-ray energy flux at T_X^* , β is the X-ray spectral index of the plateau phase in the X-ray band (Evans et al. 2009); $d_{L,\text{rec}}$ is related with the reconstructed apparent magnitude by using the ML algorithms and the absolute magnitude¹⁶. We use sub-sample at $0.553 \leq z < 1.4$ from the Platinum sample, which consists of 50 GRBs ($0.553 \leq z \leq 5.0$) to calibrate the 2D Dainotti relation. The results by KNN and RF algorithms are summarized in Table 4. We find that the calibration results by ML from D’Agostini (2005) likelihood function are consistent with those in the current works calibrated with sub-sample at $0.553 \leq z \leq 1.960$ of the Platinum sample from SNe Ia by neural networks (Mukherjee et al. 2024b): $a = -1.04 \pm 0.16$, $C_0 = 51.16 \pm 0.54$, $\sigma_{\text{int}} = 0.41 \pm 0.08$; and from OHD by a Gaussian Processes Bayesian reconstruction tool (Favale et al. 2024): $a = -1.03 \pm 0.16$, $C_0 = 51.20 \pm 0.52$, $\sigma_{\text{int}} = 0.43 \pm 0.08$.

We combine GRB data at high-redshift ($1.4 \leq z \leq 5.0$) with the calibrated 2D Dainotti relation by Reichart (2001) likelihood function to constrain cosmological parameters. The joint results from the high-redshift GRBs and OHD are summarized

¹⁵Dainotti et al. (2008; 2010; 2011; 2013; 2015) proposed the relation between the plateau luminosity and the end time of the plateau in X-ray afterglows (2D Dainotti relation) to constrain for cosmological parameters. Furthermore, Dainotti et al. (2016) proposed the 3D Dainotti relation among the rest-frame time and X-ray luminosity at the end of the plateau emission and the peak prompt luminosity with small intrinsic scatter. Cao et al. (2022a;b) investigated the 2D and 3D Dainotti relation standardized with the Platinum sample (Dainotti et al. 2020) including 50 GRB data.

¹⁶Following Mukherjee et al. (2024a;b), we fix the absolute magnitude $M = -19.35$.

Table 4 The best-fitting results (the slope a , the intercept C_0 and the intrinsic scatter σ_{int}) of the Daiotti relation at $z < 1.4$ by the likelihood method (D’Agostini 2005) and Reichart (2001).

Likelihood	Methods	Datasets	a	C_0	σ_{int}
D’Agostini (2005)	KNN	GRBs ($z < 1.4$)	$-1.08^{+0.36}_{-0.36}$	$51.70^{+1.30}_{-1.30}$	0.538
	RF	GRBs ($z < 1.4$)	$-1.07^{+0.36}_{-0.36}$	$51.70^{+1.30}_{-1.30}$	0.536
Reichart (2001)	KNN	GRBs ($z < 1.4$)	$-1.29^{+0.26}_{-0.21}$	$52.45^{+0.74}_{-0.94}$	0.463
	RF	GRBs ($z < 1.4$)	$-1.29^{+0.25}_{-0.21}$	$52.45^{+0.75}_{-0.90}$	0.447

Table 5 Joint constraints on parameters of Ω_m , h , w_0 and w_a for the flat Λ CDM model, w CDM model, and CPL model, obtained by using the KNN, RF with 40 GRBs ($z > 1.4$) + 32 OHD data.

Models	Methods	Ω_m	h	w_0	w_a	ΔAIC	ΔBIC
Λ CDM	KNN	$0.334^{+0.049}_{-0.070}$	$0.702^{+0.040}_{-0.040}$	-	-	-	-
	RF	$0.330^{+0.049}_{-0.071}$	$0.700^{+0.041}_{-0.041}$	-	-	-	-
w CDM	KNN	$0.305^{+0.080}_{-0.059}$	$0.714^{+0.051}_{-0.065}$	$-1.16^{+0.54}_{-0.46}$	-	1.7	4.0
	RF	$0.305^{+0.080}_{-0.058}$	$0.715^{+0.054}_{-0.065}$	$-1.16^{+0.45}_{-0.45}$	-	1.7	3.9
CPL	KNN	$0.344^{+0.072}_{-0.072}$	$0.707^{+0.053}_{-0.069}$	$-1.07^{+0.57}_{-0.48}$	$-0.99^{+0.58}_{-0.58}$	3.9	8.5
	RF	$0.346^{+0.058}_{-0.069}$	$0.708^{+0.054}_{-0.068}$	$-1.07^{+0.59}_{-0.48}$	$-0.99^{+0.58}_{-0.58}$	3.9	8.5

in Table 5. We find that the results are consistent with analyses that obtained in the calibration with the Amati relation by Reichart (2001) likelihood function in Tab. 3.

6 Conclusions

In this paper, we use the ML algorithms to calibrate the Amati relation from the Pantheon+ sample to obtain the GRB Hubble diagram with the A219 sample. The KNN and RF algorithms are selected to calibrate Amati relations due to the best performances. By the KNN algorithm with GRBs at $0.8 < z < 8.2$ in the A219 sample and 32 OHD, we obtained $\Omega_m = 0.329^{+0.046}_{-0.068}$, $h = 0.709^{+0.038}_{-0.038}$ for the flat Λ CDM model; $\Omega_m = 0.301^{+0.080}_{-0.057}$, $h = 0.721^{+0.048}_{-0.065}$, $w = -1.13^{+0.62}_{-0.38}$ for the flat w CDM model; and $\Omega_m = 0.341^{+0.072}_{-0.072}$, $h = 0.713^{+0.051}_{-0.051}$, $w_0 = -1.03^{+0.60}_{-0.45}$, $w_a = -0.97^{+0.58}_{-0.58}$ for the CPL model at the 1σ confidence level, which are most identical with results by the RF algorithm. These results favor a possible DE evolution ($w_a \neq 0$) at the $1\text{-}\sigma$ confidence region for both cases. We also find that the Λ CDM model is favoured respect to the w CDM model and the CPL model from the results of ΔAIC and ΔBIC . Our results with GRBs at $0.8 \leq z \leq 8.2$ are consistent with previous analyses that obtained in Liang et al. (2022); Liu et al. (2022b); Li, Zhang & Liang (2023) using GP from the Pantheon data and OHD at $z < 1.4$. Compared ML to GP, we find that KNN and RF methods with the lowest values in terms of MSE are competitive technics to GP in precision.

Furthermore, we also investigate the Dainotti relation by the ML algorithms for comparison. We find that calibration results of the 2D Dainotti relation are consistent with those in the current works (Mukherjee et al. 2024b; Favale et al. 2024); and constrain results at the high-redshift from the Dainotti relation are consistent with that obtained from the Amati relation.

It should be noted that recent observations from the Dark Energy Spectroscopic Instrument (DESI) collaboration display slight deviations from Λ CDM model, see e.g., Carloni, Luongo & Muccino (2024); Luongo & Muccino (2024); Colgáin et al. (2024). In future, GRBs could be used to set tighter constraints on cosmological models by the ML technics from recent Fermi data (Wang & Liang 2024) with much smaller scatters, as well as the data from the Chinese-French mission SVOM (the Space-based multiband astronomical Variable Objects Monitor)(Bernardini et al. 2021), which will provide a substantial enhancement of the number of GRBs with measured redshift and spectral parameters.

ACKNOWLEDGMENTS

We thank Zhen Huang, Xin Luo and Prof. Jianchao Feng, Prof. Junjin Peng for kind help and discussions. This project was supported by the Guizhou Provincial Science and Technology Foundation: QKHJC-ZK[2021] Key 020 and QKHJC-ZK[2024] general 443. P. Wu was supported by the NSFC under Grants Nos. 12275080, 12073069, and by the innovative research group of Hunan Province under Grant No. 2024JJ1006, and cultivation project for FAST scientific payoff and research achievement of CAMS-CAS.

Data Availability Data are available at the following references: the A219 sample of GRB data set from Khadka et al. (2021); Liang et al. (2022), the Pantheon+ SNe Ia sample from Scolnic et al. (2022), and the latest OHD obtained with the CC method from Moresco et al. (2020; 2022); Jiao et al. (2023) and Li, Zhang & Liang (2023).

Declarations

Competing interests The authors declare no competing interests.

Ethics approval Not applicable.

References

- Akaike, H. 1974, *ITAC*, 19, 716
- Akaike, H. 1981, *J. Econ.*, 16, 3.
- Akritas M. G., & Bershadsky M. A. 1996, *ApJ*, 470, 706
- Amati, L., D’Agostino, R., Luongo, O., Muccino, M., & Tantaló, M. 2019, *MNRAS*, 486, L46

Amati, L., Frontera, F., Tavani, M., et al. 2002, *A&A*, 390, 81

Amati, L., Guidorzi, C., Frontera, F., et al. 2008, *MNRAS*, 391, 577

Amati, L. & Della Valle 2013, *IJMPD*, 22, 1330028

Arjona, R. 2020, *JCAP*, 08, 009

Arjona, R., Lin, H.N., Nesseris, S., & Tang L. 2021, *PRD*, 103, 103513

Bargiacchi, G., Dainotti, M. G., & Capozziello, S. 2023, *MNRAS*, stad2326

Betoule, M., Kessler, R., Guy, J., et al. 2014, *A&A*, 568, A22

Busti, V. C., Clarkson, C., & Seikel, M. 2014. *MNRAS*, 441, L11

Benisty, D. 2021, *PDU*, 31, 100766

Benisty, D., Mifsud, J., Levi Said, J., & Staicova, D. 2022, [arXiv:2202.04677](https://arxiv.org/abs/2202.04677)

Bernardini, M. G., Cordier, B. & Wei, J. 2021, *Galaxies*, 9, 4

Bengaly, C., Dantas, M. A., Casarini, L. & Alcaniz, J. 2023, *EPJC*, 83, 6

Borghi, N., Moresco, M. & Cimatti, A. 2022, *ApJL*, 928, L4

Cao, S., Dainotti, M., & Ratra, B. 2022a, *MNRAS*, 512, 439

Cao, S., Khadka, N., & Ratra, B. 2022b, *MNRAS*, 510, 2928

Cao, S. & Ratra, B. 2022, *MNRAS*, 513, 5686

Cao, S. & Ratra, B. [arXiv:2404.08697](https://arxiv.org/abs/2404.08697)

Capozziello, S., & Izzo, L. 2008, *A&A*, 490, 31

Capozziello, S. & Izzo, L. 2009, *NuPhS*, 194, 206

Capozziello, S., & Izzo, L. 2010, *A&A*, 519, A73

Capozziello, S., D'Agostino, R., & Luongo, O. 2018, *MNRAS*, 476, 3924

Cardone, V. F., Capozziello, S., & Dainotti, M. G., 2009, *MNRAS*, 400, 775

Carlóni, Y., Luongo, O., & Muccino, M. [arXiv:2404.12068](https://arxiv.org/abs/2404.12068)

Chevallier, M. & Polarski, D. 2001, *IJMPD*, 10, 213

Colgáin, E. O., Dainotti, M. G., Capozziello, S., et al., [arXiv:2404.08633](https://arxiv.org/abs/2404.08633)

Cucchiara, A., Levan, A., Fox, D. B., et al. 2011, *ApJ*, 736, 7

D'Agostini, G. 2005, [arXiv: physics/0511182](#)

Dainotti, M. G., Cardone V. F., & Capozziello S. 2008, *MNRAS*, L79

Dainotti, M. G., Cardone V. F., & Capozziello S. 2010, *APJ*, 722, L215

Dainotti, M. G., Ostrowski, M., & Willingale, R. 2011, *MNRAS*, 418, 2202

Dainotti, M. G., Piedipalumbo, E., & Capozziello S. 2013, *MNRAS*, 436, 82

Dainotti, M. G., Del Vecchio, R., & Shigehiro, N. 2015, *APJ*, 800, 31

Dainotti, M. G., Postnikov, S., & Hernandez, X. 2016, *APJ*, 825, L20

Dainotti, M. G., & Amati, L., 2018, *PASP*, 130, 051001

Dainotti, M. G., et al. 2020a, *ApJ*, 904, 97

Dainotti M. G., De Simone B., Schiavone T., et al., 2021, *ApJ*, 912, 150

Dainotti, M. G., Young, S., Li, L., et al. 2022a, *ApJS*, 261, 25

Dainotti, M. G., Nielson, V., Sarracino, G., et al. 2022b, *MNRAS*, 514, 1828

Dainotti, M. G., Sarracino G., & Capozziello S. 2022c, *PASJ*, 74, 1095

Dainotti, M. G., Lenart, A. L., Chraya, A., et al. 2023, *MNRAS*, 518, 2201

Dai, Z., Liang, E., & Xu, D. 2004, *ApJ*, 612, L101

Dai, Y., Zheng, X.-G., Li, Z. X., et al. 2021, *A&A*, 651, L8

Demianski, M., & Piedipalumbo, E., 2011, *MNRAS*, 415, 3580

Demianski, M., Piedipalumbo, E., Sawant, D., & Amati, L. 2017, *A&A*, 598, A112

Demianski, M., Piedipalumbo, E., Sawant, D., & Amati, L. 2017, *A&A*, 598, A113

Demianski, M., Piedipalumbo, E., Sawant, D., & Amati, L. 2021, *MNRAS*, 506, 903

Dinda, B. R. 2023, *IJMPD*, 32, 2350079

Dirirsa, F. F., Razzaque, S., Piron, F., et al. 2019, *ApJ*, 887, 13

Dhawan, S., Alsing, J., & Vagnozzi, S. 2021, *MNRAS*, 506, L1

Escamilla-Rivera, C., Quintero, M. A. C., & Capozziello, S. 2020, *JCAP*, 03, 008

Escamilla-Rivera, C., Carvajal M., Zamora C., & Hendry M. 2022, *JCAP*, 04, 016

Evans P. A., Beardmore A. P., Page K. L. et al., 2009, *MNRAS* , 397, 1177

Favale, A., Gomez-Valent, A. & Migliaccio M. 2023, [arXiv:2301.09591](#)

Fenimore, E. E., & Ramirez-Ruiz, E. 2000, [arXiv preprint astro-ph/0004176](#)

Firmani, C., Ghisellini, G., Ghirlanda, G., & Avila-Reese, V. 2005, *MNRAS*, 360, L1

Firmani, C., Ghisellini, G., Avila-Reese, V., & Ghirlanda, G. 2006, *MNRAS*, 370, 185

Favale, A., Dainotti, M. G., Gomez-Valent, A., & Migliaccio, M. 2024, *JHEA*, 44, 323

Fluri, J., Kacprzak, T., Lucchi, A., et al. 2018, *PRD*, 98, 123518

Fluri, J., Kacprzak, T., Lucchi, A., et al. 2018, *PRD*, 100, 063514

Foreman-Mackey, D., Hogg, D. W., Lang, D., & Goodman, J. 2013, *PASP*, 125, 306

Gal, Y., & Ghahramani, Z. 2016a, [arXiv:1506.02142](#)

Gal, Y., & Ghahramani, Z. 2016b, [arXiv:1506.02157](#)

Gangopadhyay, M. R., Sami, M., Sharma, & Mohit K. 2023, *PhRvD*, 108, 103526

Gao, H., Liang, N., & Zhu, Z.-H. 2012, *IJMPD*, 21, 1250016

Ghirlanda, G., Ghisellini, G., & Lazzati, D. 2004a, *ApJ*, 616, 331

Ghirlanda, G., Ghisellini, G., Lazzati, D., & Firmani, C. 2004b, *ApJ*, 613, L13

Ghirlanda, G., Ghisellini, G., & Firmani, C. 2006, *New, J. Phys.*, 8, 123

Gómez-Valent, A., Amendola, L., 2018. *JCAP*, 1804, 051

Gomez-Valent, A. 2022, *PhRvD*, 105, 043528

Gowri G. & Shantanu D. 2022, *JCAP*, 10, 069

Hogg N.B. , Martinelli M. & Nesseris S. 2020, *JCAP*, 12, 019

Hu, J. P., Wang, F. Y., & Dai, Z. G. 2021, *MNRAS*, 507, 730

Hu, J. P. & Wang, F. Y. 2023, *Universe*, 9, 94

Izzo, L., Muccino, M., Zaninoni, E., Amati, L., & Della Valle, M. 2015, *A&A*, 582, [A115](#)

Jia, X. D., Hu, J. P., Yang, J., Zhang, B. B., & Wang, F. Y. 2022, *MNRAS*, 516, 2575

Jia, X. D., Hu, J. P. & Wang, F. Y. 2023, *A&A*, 674, A45

Jiao, K., Borghi, N., Moresco, M. & Zhang, T-J. 2023, *ApJS*, 265, 48

Jimenez, R., & Loeb, A. 2002, *ApJ*, 573, 37

Jimenez, R., Verde, L., Treu, T. & Stern, D. 2003, *ApJ*, 593, 622

Kessler, R., & Scolnic, D. 2017, *ApJ*, 836, 56

Khadka, N. & Ratra, B. 2020, *MNRAS*, 499, 391

Khadka, N., Luongo, O., Muccino, M., & Ratra, B. 2021, *JCAP*, 09, 042

Kodama, Y., Yonetoku, D., Murakami, T., et al. 2008, *MNRAS*, 391, L1

Krishnan C., Colgáin E. Ó., Ruchika S., Sheikh-Jabbari M. M., & Yang T., 2020, *PhRvD*, 102, 103525

Krishnan C., Ó Colgáin E., Sheikh-Jabbari M. M., & Yang T., 2021, *PhRvD*, 103, 103509

Kumar, D. et al. 2023, *JCAP*, 07,021

Li, H., Xia, J.-Q., Liu, J., et al. 2008, *ApJ*, 680, 92

Li, X. and Lin, H.-N., 2018. *MNRAS*, 474, 313

Li, E.-K., Du, M., & Xu, L. 2020, *MNRAS*, 491, 4960

Li, X., Keeley, R. E., Shafieloo, A., et al. 2021, *MNRAS*, 507, 919

Li, Z., Zhang, B., & Liang, N. 2023, *MNRAS*, 521, 4406

Li, J.-L., Yang, Y.-P., Yi, S.-X., Hu, J.-P., Wang, F.-Y., & Qu, Y.-K. 2023, *ApJ*, 953, 58

Liang, N., Xiao, W. K., Liu, Y., & Zhang, S. N. 2008, *ApJ*, 685, 354

Liang, N., & Zhang, S. 2008, *AIP Conf. Proc. Vol. 1065*, Am. Inst. Phys New York

Liang, N., Wu, P., & Zhang, S. N. 2010, *PRD*, 81, 083518

Liang, N., Xu, L., & Zhu, Z. H. 2011, *A&A*, 527, A11

Liang, N., Li, Z., Xie, X., & Wu, P. 2022, *ApJ*, 941, 84

Liang, E., & Zhang, B. 2005, *ApJ*, 633, 611

Liang, E., & Zhang, B. 2006, *MNRAS*, 369, L37

Lin, H. N., Li, X. & Chang, Z. 2016, *MNRAS*, 455, 2131

Lin, H. N., Li, M. H., & Li, X. 2018, *MNRAS*, 480, 3117

Linder, E.V. 2003, *PRL*, 90, 091301

Liu, Y., Chen, F., Liang, N., et al. 2022, *ApJ*, 931, 50

Liu, Y., Liang, N., Xie, X., et al. 2022, *ApJ*, 935, 7

Liu, J., & Wei, H. 2015, *GRGr*, 47, 141

Luongo, O., & Muccino, M. 2020, *A&A*, 641, A174

Luongo, O., & Muccino, M. 2021, *Galaxies*, 9, 77

Luongo, O., & Muccino, M. 2021, *MNRAS*, 503, 4581

Luongo, O., & Muccino, M. 2023, *MNRAS*, 518, 2247

Luongo, O., & Muccino, M. arXiv:2404.07070

Malekjani, M., Mc Conville, R., Colgáin, E. O, et al. 2023, arXiv:2301.12725

Montiel, A., Cabrera, J. I., & Hidalgo, J. C. 2021, *MNRAS*, 467, 3239

Moresco, M., Verde, L., Pozzetti, L., Jimenez, R. & Cimatti, A. 2012, *JCAP*, 2012, 053

Moresco, M. 2015, 450, L16

Moresco, M., Pozzetti, L., Cimatti, A. et al. 2016, *JCAP*, 2016, 014

Moresco M., Jimenez R., Verde L., et al. 2020, *ApJ*, 898, 82

Moresco M., Amati, L., Amendola, L. et al. 2022, *Living Reviews in Relativity*, 25, 6

Muccino, M., Izzo, L., Luongo, O., et al. 2021, *ApJ*, 908, 181

Muccino, M., Luongo, O., & Jain, D., 2023, *MNRAS*, 523, 4938

Mu, Y., Chang, B., & Xu, L. 2023, *JCAP*, 09, 041

Mukherjee, P., Dialektopoulos, K. F., Levi Said, J. & Mifsud, J. 2024a, *JCAP* 09, 060

Mukherjee, P., Dainotti, M. G., & Dialektopoulos, K. F. 2024b, arXiv:2411.03773

Norris, J. P., Marani, G. F., & Bonnell, J. T. 2000, *ApJ*, 534, 248

Planck Collaboration. Aghanim, N., Akrami, Y., Arroja, F., et al. 2020, *A&A*, 641, A1

Perivolaropoulos, L., & Skara, F. 2023, *MNRAS*, 520, 5110

Postnikov, S., Dainotti, M. G., Hernandez, X., & Capozziello, S. 2014, *ApJ*, 783, 126

Shah, R., Saha, S., Mukherjee, P. et al. 2024, *ApJS*, 273, 27

Ratsimbazafy, A. L., Loubser, S. I., Crawford, S. M. et al. 2017, *MNRAS*, 467, 3239

Reichart, D. E. 2001, *ApJ*, 553, 57

Riess, A. G., Yuan, W., Macri, L. M., et al. 2022, *ApJL*, 934, L7

Rumelhart, D. E., Hinton, G. E., & Williams, R. J. 1986, *Nature*, 323, 533

Santos-da-Costa, S., Busti, V. C., and Holanda, R. F. L., 2015. *JCAP*, 10, 061

Schaefer, B. E. 2003, *ApJ*, 583, L67

Schaefer, B. E. 2007, *ApJ*, 583, L67

Scolnic, D. M., Jones, D. O., Rest, A., et al. 2018, *ApJ*, 859, 101

Scolnic, et al. 2022, *ApJ*, 938, 113

Schwarz, G. 1978, *AnSta*, 6, 461

Seikel, M., Clarkson, C., & Smith, M. 2012, *JCAP*, 06, 036

Seikel, M., Yahya, S., Maartens, R., & Clarkson, C. 2012, *PRD*, 86, 083001

Seikel, M., & Clarkson, C., 2013, [arXiv:1311.6678](https://arxiv.org/abs/1311.6678)

Shirokov, S. I., Sokolov, I. V., Lovyagin, N. Yu, et al. 2020, *MNRAS*, 496, 1530

Simon, J., Verde, L. & Jimenez, R. 2005, *PhRvD*, 71, 123001

Srivastava, N., Hinton, G., Krizhevsky, A., Sutskever, I., et al. 2014, *The journal of machine learning research*, 15, 1929

Stern, D., Jimenez, R., Verde, L., Kamionkowski, M. & Starford, S. A. 2010, *JCAP*, 2010, 008

Tang L., Li X., Lin, H.-N., & Liu L. 2021, *ApJ*, 907, 121

Tang L., Lin, H.-N., Li X., & Liu L. 2022, *MNRAS*, 509, 1194

Tsutsui, R., Nakamura, T., Yonetoku, D., Murakami, T., Kodama, Y., & Takahashi, K. 2009, *JCAP*, 0908, 015

Tsutsui, R., Nakamura, T., Yonetoku, D., et al. 2009, *MNRAS*, 394, L31

Vagnozzi, S., Loeb, A., & Moresco, M. 2021, *ApJ*, 908, 84

Wang, F., & Dai, Z. G. 2006, *MNRAS*, 368, 371

Wang, Y. 2008, *PhRvD*, 78, 123532

Wang, F. Y., & Dai, Z. G. 2011, *A&A*, 536, 96

Wang, J. S., Wang, F. Y., Cheng, K. S., & Dai, Z. G. 2016, *A&A*, 585, A68

Wang, Y. Y., & Wang, F. Y. 2019, *ApJ*, 873, 39

Wang, F. Y., Hu, J. P., Zhang, G. Q., & Dai, Z. G. 2022, *ApJ*, 924, 97

Wang, G.-J., Wei, J.-J., Li, Z.-X., et al. 2017. *ApJ*, 847, 45

Wang, G.-J., Ma, X.-J., Li, S.-Y., & Xia, J.-Q. 2020. *ApJS*, 246, 13

Wang, G.-J., Ma, X.-J. & Xia, J.-Q. 2021. *MNRAS*, 501, 5714

Wang, G., Li, X., Liang, N. 2024, *ApSS*, 369, 74

Wang, H. & Liang, N. arXiv:2405.14357

Wei, H., Zhang, S. N. 2009, *EPJC*, 63, 139

Wei, H., 2010, *JCAP*, 08, 020

Wei, J.-J. & Wu, X.-F., 2017. *ApJ*, 838, 160w

Wong K. C., Suyu S. H., Chen G. C.-F., Rusu C. E., et al., 2020, *MNRAS*, 498, 1420

Xie, H., Nong, X., Wang, H., Zhang, B., Li, Z. & Liang, N. arXiv:2307.16467

Xu, D., Dai, Z., & Liang, E. 2005, *ApJ*, 633, 603

Xu, F., Tang, C.-H., Geng, J.-J., Wang, F.-Y., Wang, Y.-Y., Kuerban, A. & Huang, Y.-F. 2021, *ApJ*, 920, 135

Xu, B., Wang, Z., Zhang, K., Huang, Q. & Zhang, J. 2022, *ApJ*, 939, 115

Xu, F., Huang, Y.-F. , Geng, J.-J., et al. 2023, *A&A*, 673, A20

Yonetoku, D., Murakami, T., Nakamura, T., et al. 2004, *ApJ*, 609, 935

- Yu, B., Qi, S., & Lu, T. 2009, *ApJ*, 705, L15
- Yahya, S., Seikel, M., Clarkson, C., Maartens, R., & Smith, M. 2014. *PRD*, 89, 023503
- Yang, T, Guo, Z-K, Cai, R-G, 2015. *PRD*, 91, 123533
- Yang, T., Holanda, R. F. L., and Hu, B., 2019. *Astropart. Phys.* 108, 57-62
- Zhang, Y., 2014. [arXiv: 1408.3897](#)
- Zhang, C., Zhang, H., Yuan, S., Liu, S., Zhang, T. & Sun, Y. 2014, *RAA*, 14, 1221
- Zhang, J. C., Jiao, K., Zhang, T., Zhang, T. J., & Yu, B. 2022, *ApJ*, 936, 21
- Zhou, H., & Li, Z., 2019. *Chinese Physics C.*, 43, 035103